Microporous and Mesoporous Materials 278 (2019) 414–422

Contents lists available at ScienceDirect

Microporous and Mesoporous Materials

journal homepage: www.elsevier.com/locate/micromeso

Multilamellar and pillared titanium Silicalite-1 with long-range order of zeolite nanosheet layers: Synthesis and catalysis

Wei Wu[a], Dat T. Tran[b], Xianyuan Wu[c], Su Cheun Oh[a], Manyun Wang[d], Huiyong Chen[d], Laleh Emdadi[b], Junyan Zhang[a], Emily Schulman[a], Dongxia Liu[a,*]

[a] Department of Chemical and Biomolecular Engineering, University of Maryland, College Park, MD, 20742, USA
[b] U. S. Army Research Laboratory, RDRL-SED-E, 2800 Powder Mill Road, Adelphi, MD, 20783, USA
[c] Institute of Industrial Catalysis, Zhejiang University of Technology, Hangzhou, China
[d] School of Chemical Engineering, Northwest University, Xi'an, Shaanxi, 710069, China

ARTICLE INFO

Keywords:
Multilamellar TS-1
Pillared TS-1
Phenol hydroxylation
Cyclooctene epoxidation

ABSTRACT

Titanium silicalite-1 (TS-1) nanosheets can be synthesized from the precursor gels containing a diquaternary ammonium template in hydroxide form. The TS-1 nanosheets tend to form unilamellae interconnected in disordered aggregates. Pillaring of TS-1 nanosheets preserves the mesoporosity, but lacks long-range order of nanosheet layers. Here, we report synthesis of multilamellar TS-1 (M-TS-1) with long-range order of nanosheet layers from the precursor gels containing hexanediamine (C_6DN) and diquaternary ammonium template in bromide form ($C_{22\text{-}6\text{-}6}Br_2$). Pillaring of M-TS-1 produced pillared TS-1 (P-TS-1) with well-preserved mesoporosity and long-range order of layers. The influences of concentrations of $C_{22\text{-}6\text{-}6}Br_2$, C_6DN, and Ti precursor as well as crystallization time, on the resultant M-TS-1 were investigated. The physicochemical properties of the M-TS-1 and P-TS-1 were studied and compared to the conventional TS-1 zeolite. The presence of mesopores in P-TS-1 enhanced the catalytic performance in reactions involving bulky molecules.

1. Introduction

Zeolites are generally defined as crystalline microporous aluminosilicates, in which silicon (Si^{4+}) and aluminum (Al^{3+}) are coordinated tetrahedrally with oxygen to form various framework types and pore connectivities [1,2]. The presence of aluminum (Al^{3+}) in zeolites imposes net negative charges on the framework, which are often counterbalanced by organic/inorganic cations or protons. Therefore, zeolites are endowed with ionic exchange capability as well as Brønsted acidity, widely used for adsorption [3,4], separation [5,6], and catalysis [7,8]. Besides aluminum, other elements [9–13] also can be introduced into zeolite frameworks, which confer chemical properties different from the negative charges and consequent Brønsted acidity caused by the presence of aluminum. For example, the isomorphic substitution of titanium (Ti^{4+}) in tetrahedral coordination in zeolite frameworks offers Lewis acidity and redox properties [14–17]. Titanium silicalite-1 (TS-1), discovered by EniChem researchers by isomorphic substitution Ti^{4+} in MFI framework [18] is the first heterogeneous catalyst for the selective oxidation of hydrocarbons with hydrogen peroxide (H_2O_2) oxidizing agent in industrial processes [19–21].

Although TS-1 is an important eco-friendly industrial-scale oxidation catalyst, it is challenged in the catalytic processes involved with bulky organic molecules. The inaccessibility of molecules to active sites confined in TS-1 micropores and slow mass transport led to inferior catalytic performances [22]. Synthesis of Ti-containing zeolite polymorphs (or called titanosilicate) with large micropores have been practiced to mitigate the mass transport limitation and active site inaccessibility issues. For example, the isomorphic substitution Ti in zeolite BEA [23], MWW [24,25], UTL [26], ZSM-12 [27], ITQ-7 [28,29] and ITQ-17 [30] have been achieved, and the resultant catalysts showed improved performance in oxidation reactions. Another effort in synthesis of titanosilicate with improved mass transport and acid site accessibility is to prepare Ti-containing zeolite nanosheets. As the characteristic length of zeolites shrinks down to the single-unit-cell level to form nanosheets, the active site accessibility and mass transport can be enhanced. Thus, Ti-containing zeolite nanosheets in the MWW and FER framework types, designated as Ti-ITQ-2 [31–33] and Ti-ITQ-6 [34,35], respectively, have been prepared. Recently, the multilamellar Ti-containing MEL (TS-2) nanosheets were prepared under the assistance of mixed templates of cetyltrimethylammonium tosylate and tetramethylammonium hydroxide [36]. The Ti-containing zeolite nanosheets showed high activities in the epoxidation of cyclohexene with

---

[*] Corresponding author.
E-mail address: liud@umd.edu (D. Liu).

https://doi.org/10.1016/j.micromeso.2019.01.010
Received 14 October 2018; Received in revised form 26 December 2018; Accepted 6 January 2019

tert-butyl hydroperoxide and/or phenol hydroxylation reactions [37–40].

Other than the MWW, FER and MEL framework type of Ti-containing zeolite nanosheets, titanosilicate nanosheets of MFI framework (i.e., TS-1) have also been reported. In particular, the TS-1 nanosheets were synthesized under the assistance of a di-quaternary ammonium surfactant template in the hydroxide form [$(C_{16}H_{33}-N^+(CH_3)_2-C_6H_{12}-N^+(CH_3)_2-C_6H_{13})(OH)_2$, $C_{16\text{-}6\text{-}6}(OH)_2$] [39]. The as-obtained TS-1 nanosheets stayed as disordered thin platelets with a single unit-cell thickness. Replacement the template from $C_{16\text{-}6\text{-}6}(OH)_2$ to $(C_{22}H_{45}-N^+(CH_3)_2-C_6H_{12}-N^+(CH_3)_2-C_6H_{13})(OH)_2$ ($C_{22\text{-}6\text{-}6}(OH)_2$), extension of the synthesis time from 10 days to 20 days and temperature from 413 K to 423 K led to the formation of multilamellar TS-1 nanosheets [38]. Pillaring of multilamellar TS-1 has been explored by Přech's and Gläser's groups [37,41], but the resultant product lacks the long-range order of layered structure. It should be noted that all the previous studies used the di-quaternary ammonium template in the hydroxide-form, which was obtained by ion-exchange of template in bromide form using an anionic exchange resin.

In TS-1 synthesis, the presence of alkali metal cations, even in a very small amount, in the synthetic gel prevents incorporation of titanium into the zeolite framework [42–44]. Thus, organic templates in the hydroxide form are often employed for the synthesis process. The cationic component of the template acts as the structure directing agent, while the anionic hydroxide (OH^-) ion is the mineralization agent. In this way, the alkali metal cations in the synthesis gel can be avoided by elimination of inorganic alkali base that is often required for the zeolite crystallization [18,20,45,46]. For example, the conventional TS-1 is commonly prepared by employing the tetrapropylammonium hydroxide (TPAOH) template [47–49]. Similarly, the TS-1 nanosheets were synthesized under assistance of organic surfactant templates that were particularly ion-exchanged into hydroxide from bromide form using an anionic exchange resin [38,39]. The synthesis of TS-1 nanosheets by employing templates in other forms has not been attempted, but has potential to lower the cost by eliminating the ion-exchange step in template preparation.

In the present work, we report the synthesis of multilamellar TS-1 by directly using the di-quaternary ammonium template in bromide form ($C_{22}H_{45}-N^+(CH_3)_2-C_6H_{12}-N^+(CH_3)_2-C_6H_{13})(Br^-)_2$, $C_{22\text{-}6\text{-}6}Br_2$) and pillaring of multilamellar TS-1 to form pillared TS-1 with long-range order of nanosheet layers. A mixture of $C_{22\text{-}6\text{-}6}Br_2$ and hexanediamine (C_6DN), in which the former served as the structure directing agent and the latter provided alkalinity, was used for multilamellar TS-1 crystallization. The intercalation of tetraethyl orthosilicate (TEOS) followed by a hydrolysis in multilamellar TS-1 led to the formation of pillared TS-1. The physicochemical properties of the multilamellar TS-1 and pillared TS-1 were studied and compared to the conventional TS-1 zeolite. The preservation of mesoporosity between adjacent zeolite layers and long-range order of zeolite nanosheets in pillared TS-1 were confirmed by structural characterizations. The pillared TS-1 showed an improved active site accessibility and catalytic activity than the conventional and multilamellar TS-1 in reactions involved with bulky molecules.

2. Experimental

2.1. Materials

Titanium (IV) *n*-butoxide (TBOT, 99% purity), sodium hydroxide (NaOH, 97.0% purity), 1-butanol (BuOH, 99% purity) and tetra-n-propylammonium hydroxide (TPAOH, 40 wt% solution) were supplied by Alfa Aesar. Tetraethyl orthosilicate (TEOS, 98% purity), hexanediamine ($C_6H_{16}N_2$, 98% purity), and phenol (99% purity) were purchased from Sigma-Aldrich. Cyclooctene (95% purity) was purchased from TCI. Hydrogen peroxide (H_2O_2, 30 wt% solution) was purchased from EMD Millipore Corporation. Deionized (DI) water was used throughout the experiments. Di-quaternary ammonium surfactant template ($C_{22\text{-}6\text{-}6}Br_2$) was synthesized based on the reported method [50] and the synthesis procedure has also been explained in our previous publications [51,52].

2.2. Synthesis of multilamellar TS-1 zeolite

In a typical synthesis, 2.02 g of C_6DN was dissolved in 20 mL DI water, followed by addition of 6.16 g TEOS. The resultant mixture was magnetically stirred at room temperature until a homogeneous solution was formed. This mixture was then cooled in an iced bath, and a freshly prepared solution of 0.10 g TBOT in 0.64 g *n*-butanol was added dropwise under vigorous stirring. The above mixture was heated to 333 K, and a $C_{22\text{-}6\text{-}6}Br_2$ solution that was prepared by dissolving 1.48 g $C_{22\text{-}6\text{-}6}Br_2$ in 10.8 g DI water, was added dropwise under stirring. The resultant gel was further aged at 333 K for 3 h under stirring. The molar composition of the gel mixture was $100SiO_2/60C_6DN/7C_{22\text{-}6\text{-}6}Br_2/1TiO_2/6000H_2O/30BuOH$. Afterwards, the synthetic gel was transferred into a Teflon-lined autoclave and crystallization of zeolite was conducted at 513 K for 10 days under tumbling condition at 50 rpm. After crystallization, the zeolite sample was centrifuged, washed with DI water, and dried at 343 K overnight. One portion of the as-synthesized zeolite was calcined at 823 K for 4 h under flowing air ($1.67\ mL\ s^{-1}$) to form multilamellar TS-1, while the other portion was reserved for pillaring to form pillared TS-1 as described below. For convenience, the multilamellar TS-1 is designated as M-TS-1 in the remainder of the paper.

To study the effects of synthetic gel composition and hydrothermal synthesis time on growth of M-TS-1, the molar composition of $100SiO_2/60C_6DN/7C_{22\text{-}6\text{-}6}Br_2/1TiO_2/6000H_2O/30BuOH$ was used as a standard recipe, while the compositions of C_6DN, $C_{22\text{-}6\text{-}6}Br_2$, TBOT (Ti precursor), and hydrothermal synthesis time were varied in sequence. The as-synthesized zeolite is abbreviated as M-TS-1(x-y-z-m), where x, y, z and m are defined in the general recipe, $100SiO_2/xC_6DN/yC_{22\text{-}6\text{-}6}/zTiO_2/6000H_2O/30BuOH/m$ days. Table S1 in the Supporting Information lists the detailed composition for each M-TS-1 sample.

2.3. Synthesis of pillared TS-1 zeolite

Pillaring of the as-synthesized M-TS-1 was performed as those reported for pillaring of multilamellar MFI [52,53]. Typically, 1.0 g of the M-TS-1, prior to calcination step, was dispersed in 5.0 g TEOS. The mixture was sealed in a glass flask equipped with a septa under N_2 atmosphere, heated to 351 K in an oil bath and kept under magnetic stirring at 351 K for 24 h. The solid sample was collected by filtration and dried under ambient condition. Hydrolysis of entrapped TEOS in M-TS-1 was carried out by dispersing the sample in a NaOH aqueous solution (pH = 8). The weight ratio of NaOH aqueous solution to the solid zeolite sample was 10. After stirring at 333 K for 24 h, the sample was collected by centrifugation, washed with DI water twice, and then dried under ambient condition. Finally, the sample was calcined at 723 K for 6 h under N_2 atmosphere ($1.67\ mL\ s^{-1}$) and 823 K for 12 h under air atmosphere ($1.67\ mL\ s^{-1}$). The pillared TS-1 nanosheet structure is denoted as P-TS-1.

For comparison, the conventional TS-1 zeolite was synthesized according to a previous procedure [54]. Details on the synthesis procedure are included in S1 of the Supporting Information. The conventional TS-1 zeolite is designated as C-TS-1 for convenience of name abbreviation. All the samples, including M-TS-1, P-TS-1 and C-TS-1, were ion-exchanged three times using 1 M aqueous NH_4NO_3 (weight ratio of zeolite to NH_4NO_3 solution = 1:10) at 353 K for 4 h, and subsequently, centrifuged, washed with DI water, and dried at 343 K overnight. All samples were treated in dry air ($1.67\ mL\ s^{-1}$) by increasing the temperature from ambient to 823 K at $0.167\ K\ s^{-1}$ and holding for 4 h, prior to the characterization and catalytic tests.

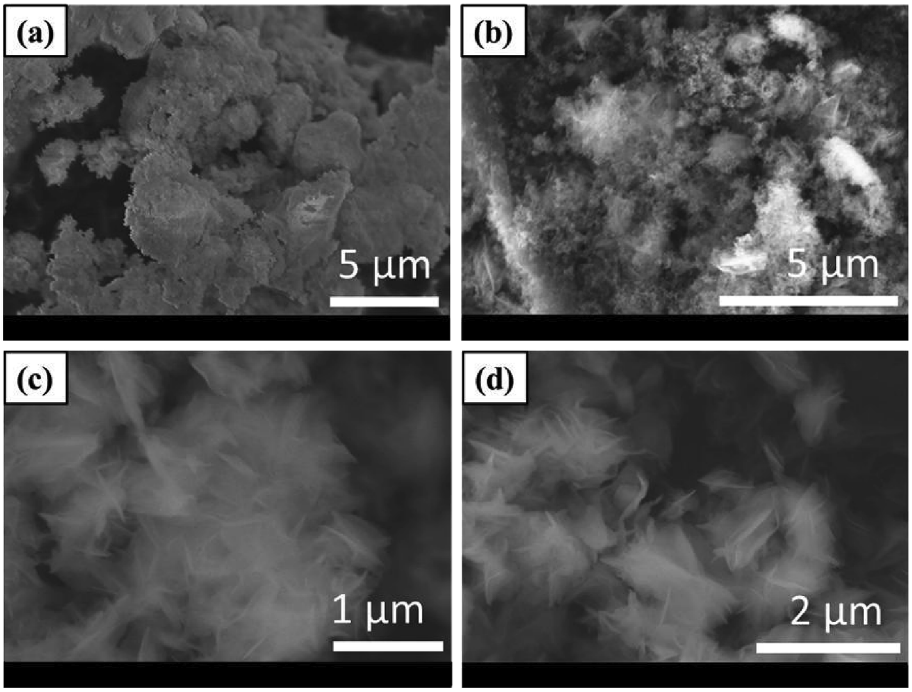

Fig. 1. SEM images of (a) M-TS-1(0-7-1-10), (b) M-TS-1(30-7-1-10), (c) M-TS-1(60-7-1-10) and (d) M-TS-1(120-7-1-10), respectively, synthesized by using different C_6DN concentrations.

2.4. Materials characterization

Powder X-Ray diffraction (XRD) patterns were recorded using a Bruker D8 Advance Lynx Powder Diffractometer (LynxEye PSD detector, sealed tube, Cu Kα radiation with Ni β-filter). Scanning electron microscopy (SEM) images were taken on a Hitachi SU-70 electron microscope to visualize the zeolite morphologies. Transmission electron microscopy (TEM) images were obtained on a JEM 2100 LaB6 electron microscope. N_2 adsorption-desorption isotherms of the samples were measured using an Autosorb-iQ analyzer (Quantachrome Instruments) at 77 K. The samples were outgassed at 573 K for 8 h at 1 mmHg pressure prior to measurements. Brunauer, Emmett and Teller (BET) method was used to determine the specific surface areas of the samples. Si and Ti contents of the zeolite samples were determined by inductively coupled plasma optical emission spectroscopy (ICP-OES, Perkin Elmer Optima 7000). Diffuse reflectance (DR) Ultraviolet-Visible (UV-Vis) spectra were obtained using an Ocean Optics USB2000+ spectrometer equipped with an IS200-4 integrating sphere detector, and the white high reflectance sphere material (manufactured from Polytetrafluoroethylene (PTFE) based bulk material) was used as the reference.

2.5. Catalytic reactions

The liquid phase phenol hydroxylation and cyclooctene epoxidation were carried out to test the catalytic performance of P-TS-1 zeolite. For comparison, the same experiments were carried out using the M-TS-1 and C-TS-1 zeolite catalyst. All reactions took place in 20 mL thick-walled glass reactors sealed with crimp tops (PTFE/silicone septum). The reactors were placed inside the holes of a copper cylinder shape incense holder that was heated on a stirring hot plate. The reactions were run at autogenous pressure and magnetic stirring (0.5-inch stirring bar, 500 rpm stirring speed) condition. For phenol hydroxylation reaction, the glass reactor was charged with 50 mg catalyst, 500 mg phenol, 10 mL DI water and 600 mg H_2O_2 (30 wt % aqueous solution) in sequence. After sealing the reactor, it was placed into a pre-heated (353 K) copper cylinder shape incense holder and kept for desired reaction time. Afterwards, the reaction was shut down by quenching the reactor in an ice bath. The reaction mixture was analyzed by a gas chromatograph (GC, Agilent 7890A) equipped with a methylsiloxane capillary column (HP-1, 50.0 m × 320 µm × 0.52 µm) connected to a flame ionization detector (FID). The cyclooctene epoxidation reaction was conducted at the same conditions except that the reaction temperature was controlled at 333 K and the reaction mixture contained 50 mg catalyst, 526 mg cyclooctene, 8 mL acetonitrile and 255 mg H_2O_2 (30 wt % aqueous solution). The representative GC micrographs for both reactions have been shown in Fig. S9 of the Supporting Information.

3. Results and discussion

3.1. Synthesis and characterization of M-TS-1 zeolites

Here, we firstly explored the synthesis of M-TS-1 nanosheets by using a mixture of $C_{22\text{-}6\text{-}6}Br_2$ and C_6DN templates, in which $C_{22\text{-}6\text{-}6}Br_2$ and C_6DN provide the structure directing agent and alkalinity functionalities, respectively. The molar composition of $100SiO_2/60C_6DN/7C_{22\text{-}6\text{-}6}/1TiO_2/6000H_2O/30BuOH$ was used as the standard recipe. The concentrations of $C_{22\text{-}6\text{-}6}Br_2$, C_6DN, TBOT (precursor of Ti), and hydrothermal growth time were varied via a series of experiments to investigate their influences on M-TS-1 crystallization and physicochemical properties. Individual experimental variables were changed, and the effects of changing these variables were investigated by comparing the products to that obtained with the standard synthesis recipe. Below, we discuss the effects of these synthesis variables in sequence.

3.1.1. Effects of C_6DN concentration

To study the effects of C_6DN on M-TS-1 synthesis, we employed the C_6DN concentration from 0 to 120, *i.e.*, x = 0, 30, 60 and 120, respectively. Fig. 1 shows the SEM images of the obtained M-TS-1 samples. The absence of C_6DN (x = 0) in the synthesis gel in Fig. 1(a) led to amorphous product, reflected by the featureless particles in the SEM image. The addition of C_6DN (x = 30 in Fig. 1(b)) promoted the growth of needle-like particles. The further increase in C_6DN content enhanced

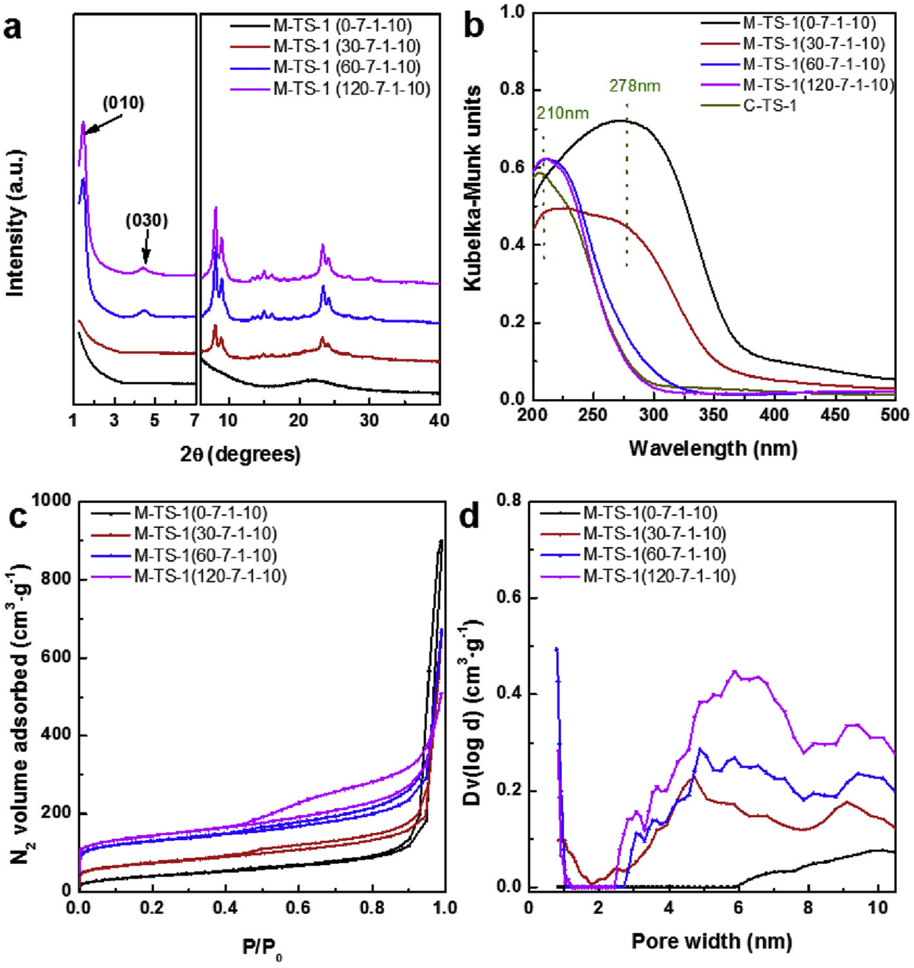

Fig. 2. (a) Low- and high-angle XRD patterns, (b) DR UV-Vis spectra, (c) N_2 isotherms and (d) NLDFT pore size distributions of M-TS-1 samples synthesized by using different C_6DN concentrations.

the TS-1 crystallization, and the product morphology transformed into nanosheet aggregates, as shown in Fig. 1(c) and (d), where x equaled to 60 and 120, respectively. The morphology of crystallized nanosheets are similar to those reported in literature by using $C_{16\text{-}6\text{-}6}(OH)_2$ templates [39].

Fig. 2 shows the physicochemical properties of TS-1 nanosheets presented in Fig. 1. The high-angle XRD peaks in Fig. 2(a) are characteristic of crystalline MFI zeolite in M-TS-1(30-7-1-10), M-TS-1(60-7-1-10) and M-TS-1(120-7-1-10) samples. The broadening in peak width around 2θ = 23.30° in M-TS-1(30-7-1-10) indicates that the material was not fully crystallized. The absence of sharp XRD diffraction peaks in M-TS-1(0-7-1-10) suggests that the sample is amorphous, consistent with the SEM data. It should be noted that no peak assigned to anatase, rutile or brookite TiO_2 phase was observed for all the samples. The low-angle XRD patterns exhibited the first-order (2θ = 1.45°) and third order (2θ = 4.50°) reflections in M-TS-1 samples synthesized with x = 60 and 120, respectively, indicating the presence of the long-range structural order of zeolite nanosheets. It should be noted that the low-angle XRD data were measured before the template removal by calcination. While with the insufficient alkalinity in the synthetic gel (x = 0 and 30), the obtained samples did not have the ordered zeolite nanosheet structure, indicated by the absence of XRD peaks at low-angle range in Fig. 2(a). The variation in C_6DN content in M-TS-1 synthesis suggests that a higher alkalinity is needed to guarantee the mineralization of zeolite framework and the long-range order of zeolite nanosheets.

The DR UV-Vis analysis was conducted to identify the coordination environment of Ti-species in the M-TS-1 samples, as shown in Fig. 2(b). For comparison, C-TS-1 sample was measured at the same condition and included in this figure. When C_6DN was not used in synthesis, a peak centered at 278 nm was observed in M-TS-1(0-7-1-10), which can be ascribed to the extra-framework Ti species [55]. When the C_6DN concentration was increased to x = 30, the band at 278 nm suppressed and a band centered at 210 nm, corresponding to tetrahedrally coordinated framework Ti-species [55], appeared. In M-TS-1(60-7-1-10) and M-TS-1(120-7-1-10) samples, the band at 278 nm completely disappeared and the band at 210 nm became sharp and significant, which is comparable to that of C-TS-1 sample. These results indicate that a high alkalinity of the synthetic gel is required to promote incorporation of Ti-species into the framework of M-TS-1 nanosheets.

The N_2 isotherms and non-local density functional theory (NLDFT) pore size distributions were used to understand the textural properties of the obtained M-TS-1 samples. The pore size distributions were calculated from the adsorption branches of N_2 isotherms by a NLDFT method, assuming an equilibrium kernel for cylindrical pores of siliceous zeolite. In Fig. 2(c), the amorphous M-TS-1(0-7-1-10) and partially crystallized M-TS-1(30-7-1-10) samples have nearly zero and $\sim 50\,cm^3\,g^{-1}$ N_2 uptake at $P/P_0 = 0.05$, while the other two M-TS-1 crystalline samples have $\sim 110\,cm^3\,g^{-1}$ N_2 adsorption at the same relative pressure. This is consistent with XRD, DR UV-vis and SEM data discussed above. The hysteresis loop in M-TS-1(120-7-1-10) sample at relative pressure range of $P/P_0 = 0.45–0.90$ is more obvious than other samples, suggesting the presence of mesopores in M-TS-1 nanosheets and change of mesopores with C_6DN content in the synthesis. Fig. 2(d) quantitatively reflects the mesoporosity change across these four samples.

3.1.2. Effects of $C_{22\text{-}6\text{-}6}Br_2$ concentration

To study the effects of $C_{22\text{-}6\text{-}6}Br_2$ concentration on M-TS-1 synthesis, the concentration of $C_{22\text{-}6\text{-}6}Br_2$ was varied from y = 1, 4, 7 to 9 in sequence. The obtained samples were named as M-TS-1(60-1-1-10), M-TS-1(60-4-1-10), M-TS-1(60-7-1-10) and M-TS-1(60-9-1-10), accordingly. The SEM images in Fig. S1 shows the sample contains featureless amorphous particles when y = 1 (Fig. S1(a)). The increase in $C_{22\text{-}6\text{-}6}Br_2$ concentration (y = 4, 7 and 9) led to crystallization of M-TS-1, reflected by the presence of nanosheet aggregates (Fig. S1(b)-(d)). The thickness of nanosheets and size of aggregates seem to increase when y was increased from 4 to 9. The XRD data in Fig. S2(a) confirmed the presence of amorphous material in M-TS-1(60-1-1-10) and crystallized TS-1 phases in the other samples. The long range ordering of the zeolite nanosheets was enhanced by the increase in $C_{22\text{-}6\text{-}6}Br_2$ concentration in the synthesis, as indicated by the sharpness of the first and third reflection peaks in the low-angle range of M-TS-1(60-7-1-10) and M-TS-1(60-9-1-10) samples, compared to M-TS-1(60-4-1-10).

Fig. S2(b) shows the coordination status of Ti-species in these four samples. Except for M-TS-1(60-1-1-10) that has both extra-framework and framework Ti-species, reflected by the presence of DR UV-Vis peaks at 268 nm and 210 nm, respectively, the other three M-TS-1 samples predominantly have tetrahedrally coordinated Ti-species. The N_2 isotherms (Fig. S2(c)) and NLDFT pore size distributions (Fig. S2(d)) further suggested the fully crystallization of M-TS-1 when the $C_{22\text{-}6\text{-}6}Br_2$ concentration was high. The existence of mesopores was found in both amorphous and crystallized M-TS-1 samples when the $C_{22\text{-}6\text{-}6}Br_2$ concentration was varied, different from the low mesoporosity in the sample synthesized with low C_6DN concentrated in Fig. S2(d).

3.1.3. Effects of TBOT concentration

In synthesis of M-TS-1 zeolites with variant Ti-species concentrations, TBOT, the Ti-precursor, was controlled as z = 1, 2, 3 and 4, respectively, in the synthesis recipe. Fig. S3 shows the SEM images of the obtained samples. All four samples have similar nanosheet aggregate morphology, suggesting that the Ti concentration did not influence the formation of TS-1 nanosheets. Fig. S4(a)-(d) present the XRD patterns, DR UV-vis spectra, N_2 isotherms and NLDFT pore size distributions of the M-TS-1(60-7-1-10), M-TS-1(60-7-2-10), M-TS-1(60-7-3-10) and M-TS-1(60-7-4-10) samples. All of them share the characteristics of XRD peaks of MFI framework and the long-range ordering of TS-1 nanosheets. They also have quite similar N_2 uptake and pore size distributions. The DR UV-vis data, however, suggest that the increase in Ti-species content in the synthesis gel led to formation of extra-framework Ti-species, indicated by the increase in peak around 300 nm in Fig. S4(b). For samples M-TS-1(60-7-1-10) and M-TS-1(60-7-2-10) that have Si/Ti ratios of 100 and 50, the DR UV-vis peaks are similar to that of C-TS-1 (Si/Ti = 100). The actual Si/Ti molar ratios are shown in Table S2, which are very close to those used in the synthesis recipe. The results indicate that Ti-species can be incorporated into the TS-1 nanosheet framework when the Si/Ti ratio was above 50, and existed as both framework and extra-framework species if the ratio is below 50. This is consistent with conventional TS-1 synthesis with variant Si/Ti ratios reported in literature [56–60].

3.1.4. Effects of hydrothermal synthesis time

The effects of hydrothermal synthesis time on TS-1 nanosheets were monitored by sampling M-TS-1(x = 60, y = 7 and z = 1) at time of m = 2, 5, 7 and 10 days, respectively. The same characterizations as those discussed above for other synthesis parameter variations were conducted on this series of samples. After 2 days of hydrothermal crystallization, the sample was still in an amorphous stage (Fig. S5(a) and Fig. S6(a)). The increase of synthesis time to 5 and 7 days has led to crystallization of TS-1 nanosheets (Figs. S5(b) and (c)). Figs. S6(c) and (d) shows the textural properties of these samples collected at different synthesis times. The high N_2 uptake and large peak in the pore size distribution plot in M-TS-1(60-7-1-2) are caused by the mesopores in the structure similar to MCM-41 material [61]. All other three samples have quite similar N_2 adsorption properties. The DR UV-vis data in Fig. S6(b) demonstrate an obvious peak centered at 284 nm in TS-1(60-7-1-2), which can be ascribed to the extra-framework Ti species [55]. When the hydrothermal synthesis time increased, the band at 284 nm suppressed and the band at 210 nm became more obvious, which was assigned to the insertion of Ti-fragments into the zeolite framework. After 7-day synthesis, the Ti-species were dominantly formed as tetrahedrally coordinated status in the zeolite framework. A combination of all these characterization data indicates that a 7-day synthesis time is sufficient for formation of M-TS-1 nanosheets, while the longer synthesis time promotes the crystallinity and formation of framework Ti-species in the obtained samples due to the solution-mediated ripening process [53]. The studies on effects of synthesis parameters on growth of multilamellar TS-1 nanosheets indicate the synthesis conditions can be optimized to form desired TS-1 nanosheet structure and composition. The as-synthesized structures have excellent long-range order of TS-1 layers, in comparison to that of TS-1 nanosheets synthesized by using templates in hydroxide form [39].

3.2. Synthesis and characterization of P-TS-1 zeolite

In order to preserve the long-range ordering structure of TS-1 nanosheets upon template removal by calcination, we synthesized P-TS-1 zeolite by the intercalation of M-TS-1 by TEOS followed by hydrolysis to form silica pillars. The TEM images in Fig. 3 shows the morphologies of the calcined P-TS-1, together with M-TS-1 and C-TS-1 samples. The C-TS-1 sample (Fig. 3(a)) consists of short cylinder-like bulk particles with an average width of ~250 nm and thickness of ~200 nm and well-crystallized smooth surfaces. The lattice fringe can be clearly seen in the TEM image of this sample (Fig. 3(b)). To show the morphology of the M-TS-1 nanosheets after calcination treatment, we selected M-TS-1

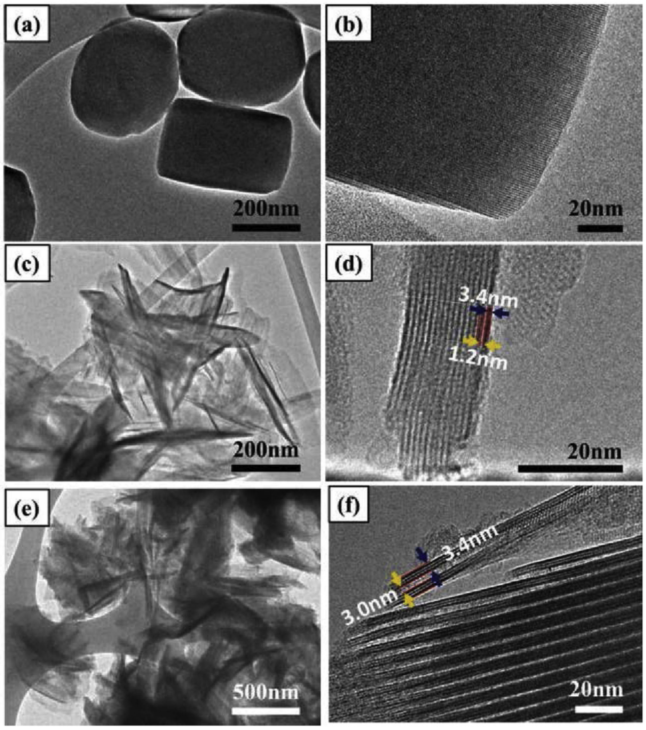

Fig. 3. TEM images of C-TS-1 (a, b), M-TS-1 (c, d) and P-TS-1 (e, f) samples, respectively. (The template in each sample has been removed by calcination treatment.)

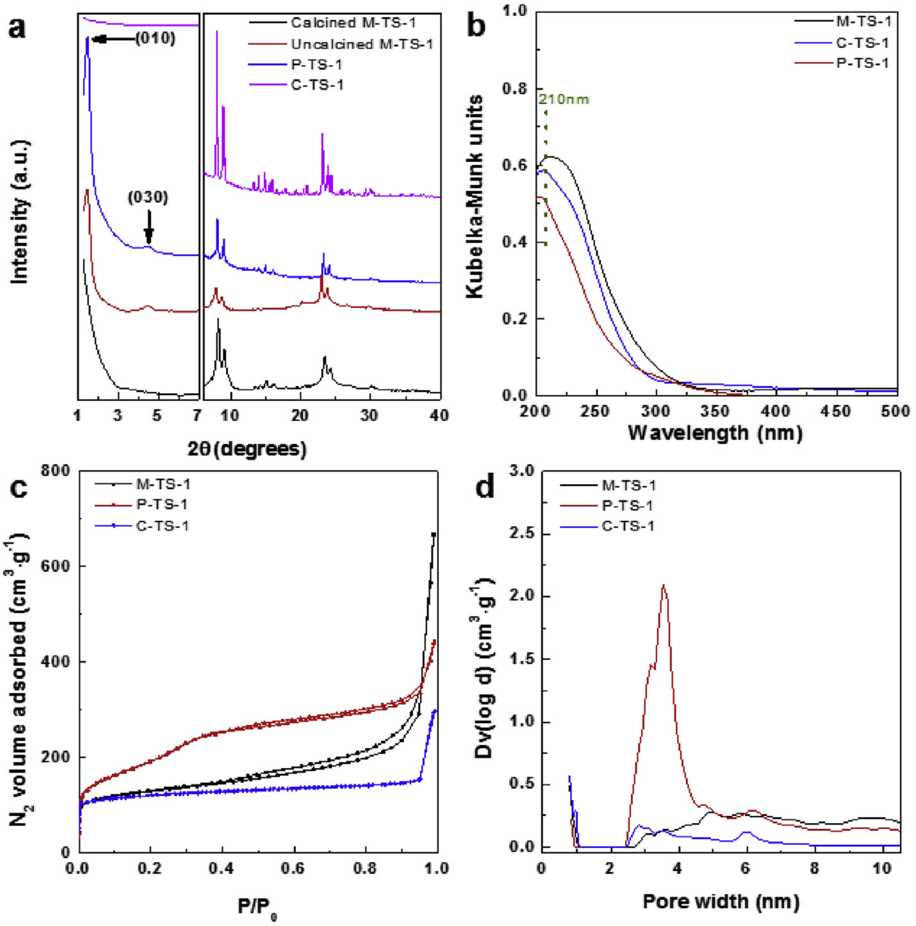

Fig. 4. (a) Low- and high-angle XRD patterns, (b) DR UV-vis spectra, (c) N_2 isotherms, (d) NLDFT pore size distributions of M-TS-1, P-TS-1 and C-TS-1 respectively. The characterization data of M-TS-1 (i.e., M-TS-1 (60-7-1-10)) is represented in each plot for comparison purpose.

(60-7-1-10) sample and examined its morphology under TEM. The sample exhibits an ordered arrangement of layered TS-1 nanosheets, but the interlayer distance is as close as ~1.2 nm (Fig. 3(c) and (d)). The P-TS-1 sample (Fig. 3(e)) has similar morphology to that of M-TS-1, but the interlayer distance was increased to 3.0 nm, as shown in Fig. 3(f), due to the inclusion of silica pillars between adjacent zeolitic TS-1 layers. For comparison purpose, more TEM images taken from M-TS-1 and P-TS-1 have been included in Fig. S7 and S8, respectively.

Fig. 4(a) shows the XRD patterns of the P-TS-1 sample, as well as those of M-TS-1 before and after calcination treatment. The pillaring treatment did not cause the formation of new materials phases or destruction of TS-1 structure since the high-angle XRD peaks are characteristic of the crystalline MFI zeolite. The low-angle XRD peaks indicate that the preservation of the layered structure after the pillaring treatment. After calcination, the layered structure in M-TS-1 was collapsed, while the structure was kept in P-TS-1 sample. The presence of both first order ($2\theta = 1.45°$) and third order ($2\theta = 4.50°$) reflections suggests the TS-1 nanosheet layers have long range ordering, very different from pillared TS-1 reported in literature [37]. The average interlayer distance between two zeolitic layers can be calculated by subtracting the thickness of the layer (along with b-axis direction of MFI, ~3.4 nm) from interlayer spacing distance that was calculated from Bragg's law, which was around 2.8 nm, consistent with the HR-TEM observation.

From the DR UV-Vis spectra in Fig. 4(b), the pillaring did not influence the coordination environment of Ti-species since the absorption peak of P-TS-1 is similar to that of C-TS-1 and M-TS-1 samples. The sharp and narrow band at 210 nm observed in the DR UV-Vis spectra indicated that the Ti-species stayed with tetrahedral coordination structure in the zeolite framework. The textural properties of TS-1 zeolites were analyzed using N_2 isotherms and the results were shown in Fig. 4(c). The C-TS-1 has a type II isotherm, while M-TS-1 and P-TS-1 have type IV isotherm with hysteresis loops. The NLDFT pore size distributions (Fig. 4(d)) of these samples determined from the adsorption branches of their isotherms illustrate that P-TS-1 has a very strong peak centered at ~3.8 nm, in comparison with M-TS-1 and C-TS-1 samples. Table S2 in the Supporting Information summarizes the textural properties of all the C-TS-1, M-TS-1 and P-TS-1 samples that were determined from the N_2 isotherms. It can be seen that the external surface area (S_{ext}), mesopore volume (V_{meso}), total pore volume (V_t) and BET surface area (S_{BET}) were dramatically increased after pillaring treatment of M-TS-1 zeolite.

3.3. Catalytic performance of P-TS-1 zeolite

Alkali metal cations in the TS-1 synthetic gel prevent incorporation of titanium into the zeolite framework [42,43]. The organic templates in hydroxide form can be obtained by reaction of quaternary ammonium halide with silver oxide, by ion-exchange with potassium hydroxide, or electro-electrodialysis [62,63]. All of these methods, however, require additional processing steps. Attempts have been made to replace quaternary ammonium hydroxide with a mixture of quaternary ammonium halide and amine or diamine in the conventional TS-1 synthesis. The resultant TS-1 products, however, often have inferior catalytic performance that has been ascribed to the large size of TS-1 crystals or low content of active Ti species in TS-1 zeolites [55,64–66]. Since the template in bromide form was used in our study, we examined the catalytic performance of M-TS-1 and P-TS-1 nanosheets to

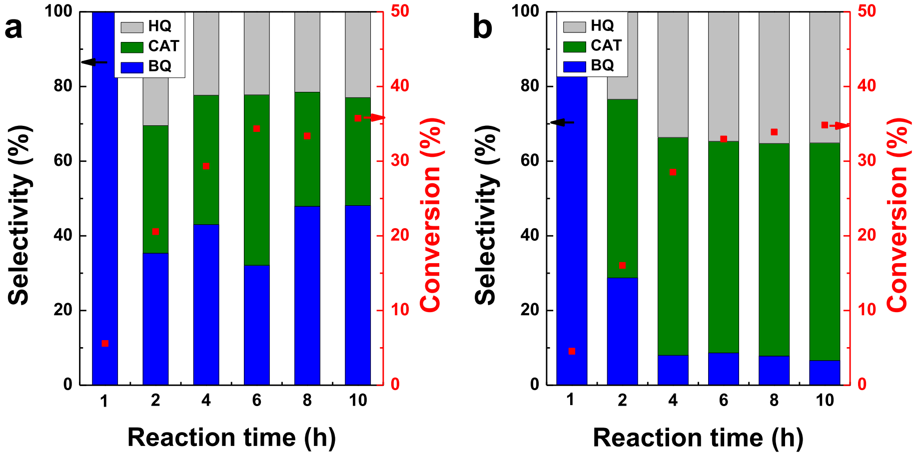

Fig. 5. Phenol conversion and product selectivity over (a) M-TS-1 and (b) P-TS-1 catalysts as a function of reaction time. (Reaction condition: 353 K, 50 mg catalyst, 500 mg phenol, 600 mg H_2O_2, 10 mL DI water. BQ: benzoquinone. CAT: catechol. HQ: hydroquinone).

understand if their activity is influenced by the aforementioned reasons. For comparison purpose, the same reactions were run over C-TS-1 zeolite.

3.3.1. *Phenol hydroxylation reaction*

The phenol hydroxylation in the presence of H_2O_2 oxidant has been studied extensively to produce catechol (CAT) and hydroquinone (HQ) that are widely used in industry as important intermediates for synthesis of medicines, perfumes, inks, polymer inhibitors, *etc.* [67–70]. TS-1 zeolite has been studied as a heterogeneous catalyst for phenol hydroxylation, which showed excellent catalytic activity [9,18,71,72]. Here, we firstly employed this reaction to test the catalytic performance of synthesized P-TS-1 catalyst. Fig. 5 and Fig. S10(a) shows the phenol conversion and product selectivity as a function of the reaction time. The phenol conversion (f) is calculated by the equation, $f = \frac{C_0 - C}{C_0} \times 100\%$, where C_0 and C are the initial and local concentrations (mol mL^{-1}) of phenol, respectively. The product selectivity (S_i) is defined as $S_i = \frac{C_i}{C_{CAT} + C_{HQ} + C_{BQ}}$x100%, where C_i is the product (i) concentration (mol mL^{-1}), i is the product type, i.e., CAT, HQ, or benzoquinone (BQ) byproduct.

The phenol conversion increased with reaction time over either P-TS-1 or M-TS-1 zeolite catalyst, as shown in Fig. 5(a) and (b). The M-TS-1 led to slightly higher conversion than P-TS-1 catalyst at each reaction time. Fig. S10(a) presents the phenol conversion and product selectivity in the same reaction occurred on C-TS-1 zeolite, which has compelling performance to that of M-TS-1 or P-TS-1. It is known that the kinetic diameter of phenol [73,74] is comparable to the micropore size (0.56 nm × 0.53 nm straight channel and 0.55 nm × 0.51 nm zigzag channel) [75] of TS-1. The reaction can take place in both micro- and mesopores of TS-1 zeolite. The slightly inferior performance of P-TS-1 to M-TS-1 in Fig. 5 could be due to the low concentration of Ti sites in the former sample, as indicated by the elemental composition of samples in Table S2 in the supporting information. The same reason leads to slightly higher phenol conversion in C-TS-1 than P-TS-1 zeolite. In addition, the location of Ti sites, within micropores versus on external surface or mesopores, in TS-1 zeolites could contribute to the differences in phenol conversion [38,39]. To verify these explanations, we have purposely synthesized M-TS-1 and C-TS-1 samples that have the same Si/Ti ratio as that of P-TS-1. As shown in Fig. S11, M-TS-1 and P-TS-1 have comparable catalytic performance, and this performance is slightly inferior to C-TS-1 in the phenol hydroxylation. For C-TS-1 or M-TS-1 with different Si/Ti ratios, the one with lower Si/Ti ratio, i.e., higher Ti content, has higher phenol conversion. Fig. 5(a) and (b) also illustrate the product selectivity as a function of reaction time and catalyst type. In the initial stage of the reaction, BQ selectivity was high and decreased with the reaction time. This phenomenon could be caused by the high concentration of H_2O_2 oxidant in the beginning of the reaction since BQ is the by-product from sequential oxidation of HQ product [76–78]. With the progress of reaction, the sum of CAT and HQ selectivities was > 95% in P-TS-1 zeolite. The selectivity comparison between these two TS-1 zeolites shows that P-TS-1 slightly favors bulkier CAT product, which might be due to its large mesoporosity. Overall, the phenol hydroxylation reaction indicates that P-TS-1 synthesized by using $C_{22\text{-}6\text{-}6}Br_2$ and C_6DN templates is active in catalytic oxidation reaction.

3.3.2. *Cyclooctene epoxidation reaction*

The phenol hydroxylation indicated the catalytic activity of active sites in the synthesized P-TS-1 zeolite, but the reaction takes place in both micro- and mesopores of the catalyst. To demonstrate the catalytic capability of P-TS-1 in processing bulky reactant molecules, we studied the cyclooctene epoxidation in the presence of H_2O_2 oxidant. Epoxidation is an important reaction for production of both fine and commodity chemicals, such as resins, plasticizers, *etc.* [79–84]. For example, the epoxycyclooctane product from the cyclooctene epoxidation can be used as key building in organic synthesis and pharmaceuticals [80,85,86].

Fig. 6(a) and (b) as well as Fig. S10(b) showed the conversion of cyclooctene as a function of reaction time and catalyst type. The increase in reaction time led to higher cyclooctene conversion. Different from the phenol hydroxylation reaction, P-TS-1 (Fig. 6(b)) had a much higher conversion than that of M-TS-1 (Fig. 6(a)) and then C-TS-1 (Fig. S10(b)) zeolite, due to the catalytic activity is restricted on the external surface. It should be noted that P-TS-1 has higher Si/Ti ratio than that of M-TS-1 and C-TS-1 samples. If all the samples have the same Si/Ti ratio in this reaction, the advantage of P-TS-1 in promoting the reaction of bulky molecules will be even more obvious. The P-TS-1 possessed a higher epoxide selectivity. This was attributed to the advantage of uniform mesoporous structure and the long-range ordering structure. When the epoxide was generated, it was easier to diffuse out from the external surface to uniform mesopores network, which consequently resulted in epoxide ring open possibility suppression and epoxide selectivity increase.

4. Conclusions

By employing a mixture of $C_{22\text{-}6\text{-}6}Br_2$ and C_6DN templates, TS-1 nanosheets with multiple layers assembled in a long-range order were successfully synthesized. The effects of $C_{22\text{-}6\text{-}6}Br_2$ and C_6DN concentrations, Ti precursor content, as well as synthesis time on structural and textural properties of M-TS-1 nanosheets were investigated. An

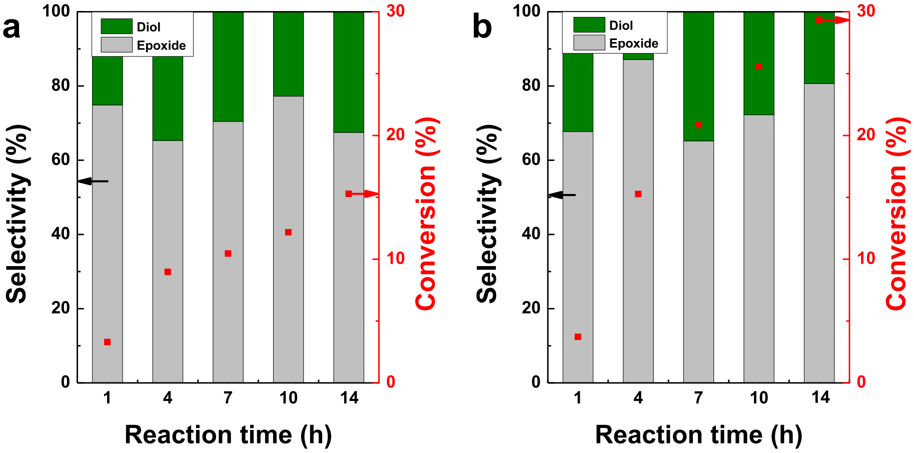

Fig. 6. Cyclooctene conversion and product selectivity over (a) M-TS-1 and (b) P-TS-1 catalysts as a function of reaction time. (Reaction condition: 333 K, 50 mg catalyst, 526 mg cyclooctene, 255 mg H_2O_2, 8 mL acetonitrile. Epoxide: cyclooctene oxide. Diol: 1,2-cyclooctanediol).

increase in $C_{22\text{-}6\text{-}6}Br_2$ and/or C_6DN concentration promoted the crystallization and long-range order of M-TS-1 nanosheets. High concentration of Ti-precursor in the synthesis gel led to formation of extra-framework Ti-species. A synthesis time of 7 days is required to crystallize the M-TS-1 nanosheets from the synthetic gel. The pillaring treatment of M-TS-1 before template removal led to preservation of mesoporosity and long-range order of layered structure in P-TS-1 zeolite. The P-TS-1 shows superior catalytic activity to M-TS-1 and C-TS-1 zeolites in reaction involving bulky molecules.

Acknowledgements

This material is based upon work supported by, or in part by, the U. S. Army Research Laboratory and the U. S. Army Research Office under contract/grant number: W911NF-17-1-0363. This project was also partially supported by National Science Foundation (grant no. CBET 1705284). W. Wu acknowledges the assistance from Dr. Sz-Chian Liou for the SEM and TEM observation of zeolite samples in this work.

Appendix A. Supplementary data

Supplementary data to this article can be found online at https://doi.org/10.1016/j.micromeso.2019.01.010.

References

[1] C.S. Cundy, P.A. Cox, The hydrothermal synthesis of zeolites: history and development from the earliest days to the present time, Chem. Rev. 103 (2003) 663–702.
[2] M.E. Davis, Ordered porous materials for emerging applications, Nature 417 (2002) 813–821.
[3] J. Pérez-Ramírez, C.H. Christensen, K. Egeblad, C.H. Christensen, J.C. Groen, Hierarchical zeolites: enhanced utilisation of microporous crystals in catalysis by advances in materials design, Chem. Soc. Rev. 37 (2008) 2530–2542.
[4] Z.L. Hua, J. Zhou, J.L. Shi, Recent advances in hierarchically structured zeolites: synthesis and material performances, Chem. Commun. 47 (2011) 10536–10547.
[5] Z. Lai, G. Bonilla, I. Diaz, J.G. Nery, K. Sujaoti, M.A. Amat, E. Kokkoli, O. Terasaki, R.W. Thompson, M. Tsapatsis, D.G. Vlachos, Microstructural optimization of a zeolite membrane for organic vapor separation, Science 300 (2003) 456–460.
[6] M.Y. Jeon, D. Kim, P. Kumar, P.S. Lee, N. Rangnekar, P. Bai, M. Shete, B. Elyassi, H.S. Lee, K. Narasimharao, S.N. Basahel, S. Al-Thabaiti, W. Xu, H.J. Cho, E.O. Fetisov, R. Thyagarajan, R.F. DeJaco, W. Fan, K.A. Mkhoyan, J.I. Siepmann, M. Tsapatsis, Ultra-selective high-flux membranes from directly synthesized zeolite nanosheets, Nature 543 (2017) 690–694.
[7] J. Čejka, G. Centi, J. Perez-Pariente, W.J. Roth, Zeolite-based materials for novel catalytic applications: opportunities, perspectives and open problems, Catal. Today 179 (2012) 2–15.
[8] M. Yoshizawa, J.K. Klosterman, Molecular architectures of multi-anthracene assemblies, Chem. Soc. Rev. 43 (2014) 1885–1898.
[9] G. Bellussi, R. Millini, P. Pollesel, C. Perego, Zeolite science and technology at Eni, New J. Chem. 40 (2016) 4061–4077.
[10] L. Meng, X. Zhu, E.J.M. Hensen, Stable Fe/ZSM-5 nanosheet zeolite catalysts for the oxidation of benzene to phenol, ACS Catal. 7 (2017) 2709–2719.
[11] P.Y. Dapsens, C. Mondelli, J. Pérez-Ramírez, Design of Lewis-acid centres in zeolitic matrices for the conversion of renewables, Chem. Soc. Rev. 44 (2015) 7025–7043.
[12] H.Y. Luo, L. Bui, W.R. Gunther, E. Min, Y. Román-Leshkov, Synthesis and catalytic activity of Sn-MFI nanosheets for the baeyer–villiger oxidation of cyclic ketones, ACS Catal. 2 (2012) 2695–2699.
[13] M. Moliner, State of the art of Lewis acid-containing zeolites: lessons from fine chemistry to new biomass transformation processes, Dalton Trans. 43 (2014) 4197–4208.
[14] M. Moliner, A. Corma, Advances in the synthesis of titanosilicates: from the medium pore TS-1 zeolite to highly-accessible ordered materials, Microporous Mesoporous Mater. 189 (2014) 31–40.
[15] C. Perego, A. Carati, P. Ingallina, M.A. Mantegazza, G. Bellussi, Production of titanium containing molecular sieves and their application in catalysis, Appl. Catal., A 221 (2001) 63–72.
[16] B. Yang, J.-G. Jiang, K. Zhang, P. Wu, Synthesis of novel titanosilicate catalysts by simultaneous isomorphous substitution and interlayer expansion of zeolitic layered silicates, Chem. Mater. 28 (2016) 5295–5303.
[17] R. Murugavel, W. Roesky Herbert, Titanosilicates: recent developments in synthesis and use as oxidation catalysts, Angew. Chem. Int. Ed. 36 (2003) 477–479.
[18] M. Taramasso, G. Perego, B. Notari, Preparation of Porous Crystalline Synthetic Material Comprised of Silicon and Titanium Oxides, US, (1983) US4410501A.
[19] M.G. Clerici, P. Ingallina, Oxidation reactions with in situ generated oxidants, Catal. Today 41 (1998) 351–364.
[20] M.G. Clerici, G. Bellussi, U. Romano, Synthesis of propylene oxide from propylene and hydrogen peroxide catalyzed by titanium silicalite, J. Catal. 129 (1991) 159–167.
[21] A. Cesana, M.A. Mantegazza, M. Pastori, A study of the organic by-products in the cyclohexanone ammoximation, J. Mol. Catal. Chem. 117 (1997) 367–373.
[22] C.G. Li, Y.Q. Lu, H.H. Wu, P. Wu, M.Y. He, A hierarchically core/shell-structured titanosilicate with multiple mesopore systems for highly efficient epoxidation of alkenes, Chem. Commun. 51 (2015) 14905–14908.
[23] M.A. Camblor, A. Corma, A. Martinez, J. Pérez-Pariente, Synthesis of a titaniumsilicoaluminate isomorphous to zeolite beta and its application as a catalyst for the selective oxidation of large organic molecules, J. Chem. Soc., Chem. Commun. 0 (1992) 589–590.
[24] P. Wu, T. Tatsumi, T. Komatsu, T. Yashima, Hydrothermal synthesis of a novel titanosilicate with MWW topology, Chem. Lett. 29 (2000) 774–775.
[25] P. Wu, T. Tatsumi, T. Komatsu, T. Yashima, A novel titanosilicate with MWW structure. I. hydrothermal synthesis, elimination of extraframework titanium, and characterizations, J. Phys. Chem. B 105 (2001) 2897–2905.
[26] J. Přech, J. Čejka, UTL titanosilicate: an extra-large pore epoxidation catalyst with tunable textural properties, Catal. Today 277 (2016) 2–8.
[27] A. Tuel, Synthesis, characterization, and catalytic properties of the new TiZSM-12 zeolite, Zeolites 15 (1995) 236–242.
[28] M.-J. Díaz-Cabañas, L.A. Villaescusa, M.A. Camblor, Synthesis and catalytic activity of Ti-ITQ-7: a new oxidation catalyst with a three-dimensional system of large pore channels, Chem. Commun. 0 (2000) 761–762.
[29] A. Corma, M.J. Díaz-Cabañas, M.E. Domine, F. Rey, Ultra fast and efficient synthesis of Ti-ITQ-7 and positive catalytic implications, Chem. Commun. 0 (2000) 1725–1726.
[30] M. Moliner, P. Serna, Á. Cantín, G. Sastre, M.J. Díaz-Cabañas, A. Corma, Synthesis of the Ti−Silicate form of BEC polymorph of β-zeolite assisted by molecular modeling, J. Phys. Chem. C 112 (2008) 19547–19554.
[31] A. Corma, U. Díaz, V. Fornés, J.L. Jordá, M. Domine, F. Rey, Ti/ITQ-2, a new material highly active and selective for the epoxidation of olefins with organic hydroperoxides, Chem. Commun. 0 (1999) 779–780.
[32] P. Serna, L.A. Baumes, M. Moliner, A. Corma, Combining high-throughput experimentation, advanced data modeling and fundamental knowledge to develop catalysts for the epoxidation of large olefins and fatty esters, J. Catal. 258 (2008) 25–34.
[33] P. Wu, D. Nuntasri, J. Ruan, Y. Liu, M. He, W. Fan, O. Terasaki, T. Tatsumi,

Delamination of Ti-MWW and high efficiency in epoxidation of alkenes with various molecular sizes, J. Phys. Chem. B 108 (2004) 19126–19131.
[34] A. Corma, U. Diaz, M.E. Domine, V. Fornés, Ti-ferrierite and TiITQ-6: synthesis and catalytic activity for the epoxidation of olefins with H_2O_2, Chem. Commun. 0 (2000) 137–138.
[35] A. Corma, U. Diaz, M.E. Domine, V. Fornés, New aluminosilicate and titanosilicate delaminated materials active for acid catalysis, and oxidation reactions using H_2O_2, J. Am. Chem. Soc. 122 (2000) 2804–2809.
[36] H.L. Chen, S.W. Li, Y.M. Wang, Synthesis and catalytic properties of multilayered MEL-type titanosilicate nanosheets, J. Mater. Chem. 3 (2015) 5889–5900.
[37] J. Přech, P. Eliášová, D. Aldhayan, M. Kubů, Epoxidation of bulky organic molecules over pillared titanosilicates, Catal. Today 243 (2015) 134–140.
[38] J. Wang, L. Xu, K. Zhang, H. Peng, H. Wu, J.-g. Jiang, Y. Liu, P. Wu, Multilayer structured MFI-type titanosilicate: synthesis and catalytic properties in selective epoxidation of bulky molecules, J. Catal. 288 (2012) 16–23.
[39] K. Na, C. Jo, J. Kim, W.-S. Ahn, R. Ryoo, MFI titanosilicate nanosheets with single-unit-cell thickness as an oxidation catalyst using peroxides, ACS Catal. 1 (2011) 901–907.
[40] J. Kim, J. Chun, R. Ryoo, MFI zeolite nanosheets with post-synthetic Ti grafting for catalytic epoxidation of bulky olefins using H_2O_2, Chem. Commun. 51 (2015) 13102–13105.
[41] N. Wilde, J. Prech, M. Pelz, M. Kubu, J. Cejka, R. Glaser, Accessibility enhancement of TS-1-based catalysts for improving the epoxidation of plant oil-derived substrates, Catal Sci Technol 6 (2016) 7280–7288.
[42] J.G. Wang, Y.B. Wang, H.Z. Chen, J.S. Lim, T. Tatsumi, Y.L. Zhao, Cation-exchange resin towards low-cost synthesis of high-performance TS-1 zeolites in the presence of alkali-metal ions, RSC Adv. 6 (2016) 15615–15621.
[43] C.B. Khouw, M.E. Davis, Catalytic activity of Titanium Silicates synthesized in the presence of alkali-metal and alkaline-earth ions, J. Catal. 151 (1995) 77–86.
[44] B. Sulikowski, J. Klinowski, Preparation and characterization of titanosilicates with ZSM-5 structure, Appl. Catal., A 84 (1992) 141–153.
[45] L. Emdadi, D.X. Liu, One-step dual template synthesis of hybrid lamellar-bulk MFI zeolite, J. Mater. Chem. 2 (2014) 13388–13397.
[46] X. Zhang, D. Liu, D. Xu, S. Asahina, K.A. Cychosz, K.V. Agrawal, Y. Al Wahedi, A. Bhan, S. Al Hashimi, O. Terasaki, M. Thommes, M. Tsapatsis, Synthesis of self-pillared zeolite nanosheets by repetitive branching, Science 336 (2012) 1684.
[47] A. Thangaraj, M.J. Eapen, S. Sivasanker, P. Ratnasamy, Studies on the synthesis of titanium silicalite, TS-1, Zeolites 12 (1992) 943–950.
[48] S. Gontier, A. Tuel, Synthesis of titanium silicalite-1 using amorphous SiO_2 as silicon source, Zeolites 16 (1996) 184–195.
[49] A.J.H.P. van der Pol, J.H.C. van Hooff, Parameters affecting the synthesis of titanium silicalite 1, Appl. Catal., A 92 (1992) 93–111.
[50] M. Choi, K. Na, J. Kim, Y. Sakamoto, O. Terasaki, R. Ryoo, Stable single-unit-cell nanosheets of zeolite MFI as active and long-lived catalysts, Nature 461 (2009) 246.
[51] L. Emdadi, Y. Wu, G. Zhu, C.-C. Chang, W. Fan, T. Pham, R.F. Lobo, D. Liu, Dual template synthesis of meso- and microporous MFI zeolite nanosheet assemblies with tailored activity in catalytic reactions, Chem. Mater. 26 (2014) 1345–1355.
[52] D. Liu, A. Bhan, M. Tsapatsis, S. Al Hashimi, Catalytic behavior of brønsted acid sites in MWW and MFI zeolites with dual meso- and microporosity, ACS Catal. 1 (2011) 7–17.
[53] K. Na, M. Choi, W. Park, Y. Sakamoto, O. Terasaki, R. Ryoo, Pillared MFI zeolite nanosheets of a single-unit-cell thickness, J. Am. Chem. Soc. 132 (2010) 4169–4177.
[54] H. Zhang, Y. Liu, Z. Jiao, M. He, P. Wu, Hydrothermal synthesis of titanium silicalite-1 structurally directed by hexamethyleneimine, Ind. Eng. Chem. Res. 48 (2009) 4334–4339.
[55] A. Tuel, Crystallization of titanium silicalite-1 (TS-1) from gels containing hexanediamine and tetrapropylammonium bromide, Zeolites 16 (1996) 108–117.
[56] W.B. Fan, R.G. Duan, T. Yokoi, P. Wu, Y. Kubota, T. Tatsumi, Synthesis, crystallization mechanism, and catalytic properties of titanium-rich TS-1 free of extraframework titanium species, J. Am. Chem. Soc. 130 (2008) 10150–10164.
[57] M. Signorile, V. Crocellà, A. Damin, B. Rossi, C. Lamberti, F. Bonino, S. Bordiga, Effect of Ti speciation on catalytic performance of TS-1 in the hydrogen peroxide to propylene oxide reaction, J. Phys. Chem. C 122 (2018) 9021–9034.
[58] Y. Zuo, M. Liu, T. Zhang, L.W. Hong, X.W. Guo, C.S. Song, Y.S. Chen, P.Y. Zhu, C. Jaye, D. Fischer, Role of pentahedrally coordinated titanium in titanium silicalite-1 in propene epoxidation, RSC Adv. 5 (2015) 17897–17904.
[59] J. Wang, Y. Zhao, T. Yokoi, N. Kondo Junko, T. Tatsumi, High-performance titanosilicate catalyst obtained through combination of liquid-phase and solid-phase transformation mechanisms, ChemCatChem 6 (2014) 2719–2726.
[60] D.G. Huang, X.A. Zhang, B.H. Chen, Z.S. Chao, Ethanol-assistant synthesis of TS-1 containing no extra-framework Ti species, Catal. Today 158 (2010) 510–514.
[61] C.T. Kresge, M.E. Leonowicz, W.J. Roth, J.C. Vartuli, J.S. Beck, Ordered mesoporous molecular-sieves synthesized by a liquid-crystal template mechanism, Nature 359 (1992) 710–712.
[62] H. Feng, C. Huang, T. Xu, Production of tetramethyl ammonium hydroxide using bipolar membrane electrodialysis, Ind. Eng. Chem. Res. 47 (2008) 7552–7557.
[63] J. Shen, J. Yu, L. Liu, J. Lin, B. Van der Bruggen, Synthesis of quaternary ammonium hydroxide from its halide salt by bipolar membrane electrodialysis (BMED): effect of molecular structure of ammonium compounds on the process performance, J. Chem. Technol. Biotechnol. 89 (2014) 841–850.
[64] G. Li, X.W. Guo, X.S. Wang, Q. Zhao, X.H. Bao, X.W. Han, L.W. Lin, Synthesis of titanium silicalites in different template systems and their catalytic performance, Appl. Catal., A 185 (1999) 11–18.
[65] Q. Zhao, X.H. Bao, X.W. Han, X.M. Liu, D.L. Tan, L.W. Lin, X.W. Guo, G. Li, X.S. Wang, Studies on the crystallization process of titanium silicalite-1 (TS-1) synthesized using tetrapropylammonium bromide as a template, Mater. Chem. Phys. 66 (2000) 41–50.
[66] X.S. Wang, X.W. Guo, G. Li, Synthesis of titanium silicalite (TS-1) from the TPABr system and its catalytic properties for epoxidation of propylene, Catal. Today 74 (2002) 65–75.
[67] L.J. Jian, C. Chen, F. Lan, S.J. Deng, W.M. Xiao, N. Zhang, Catalytic activity of unsaturated coordinated Cu-MOF to the hydroxylation of phenol, Solid State Sci. 13 (2011) 1127–1131.
[68] R. Klaewkla, S. Kulprathipanja, P. Rangsunvigit, T. Rirksomboon, W. Rathbun, L. Nemeth, Kinetic modelling of phenol hydroxylation using titanium and tin silicalite-1s: effect of tin incorporation, Chem. Eng. J. 129 (2007) 21–30.
[69] X.L. Liang, R.G. Yang, G.Y. Li, C.W. Hu, Phenol hydroxylation over Fe-incorporated mesoporous materials prepared by coprecipitation, Microporous Mesoporous Mater. 182 (2013) 62–72.
[70] D.P. Das, R.K. Barik, J. Das, P. Mohapatra, K.M. Parida, Visible light induced photo-hydroxylation of phenol to catechol over RGO-Ag_3VO_4 nanocomposites without the use of H_2O_2, RSC Adv. 2 (2012) 7377–7379.
[71] A. Tuel, S. Moussa-Khouzami, Y.B. Taarit, C. Naccache, Hydroxylation of phenol over TS-1: surface and solvent effects, J. Mol. Catal. 68 (1991) 45–52.
[72] J. Přech, Catalytic performance of advanced titanosilicate selective oxidation catalysts - a review, Catal. Rev. Sci. Eng. 60 (2018) 71–131.
[73] B. Koubaissy, J. Toufaily, M. El-Murr, T. Jean Daou, H. Hafez, G. Joly, P. Magnoux, T. Hamieh, Adsorption kinetics and equilibrium of phenol drifts on three zeolites, Cent. Eur. J. Eng. 2 (2012) 435–444.
[74] M.V. Opanasenko, M.V. Shamzhy, C. Jo, R. Ryoo, J. Čejka, Annulation of phenols: catalytic behavior of conventional and 2D zeolites, ChemCatChem 6 (2014) 1919–1927.
[75] Y. He, T.C. Hoff, L. Emdadi, Y. Wu, J. Bouraima, D. Liu, Catalytic consequences of micropore topology, mesoporosity, and acidity on the hydrolysis of sucrose over zeolite catalysts, Catal. Sci. Technol. 4 (2014) 3064–3073.
[76] J. Wang, J.N. Park, H.C. Jeong, K.S. Choi, X.Y. Wei, S.I. Hong, C.W. Lee, Cu^{2+}-exchanged zeolites as catalysts for phenol hydroxylation with hydrogen peroxide, Energy Fuels 18 (2004) 470–476.
[77] L.L. Lou, S.X. Liu, CuO-containing MCM-48 as catalysts for phenol hydroxylation, Catal. Commun. 6 (2005) 762–765.
[78] G.Q. Wu, J.H. Xiao, L. Zhang, W.J. Wang, Y.P. Hong, H.J. Huang, Y. Jiang, L. Lia, C.R. Wang, Copper-modified TS-1 catalyzed hydroxylation of phenol with hydrogen peroxide as the oxidant, RSC Adv. 6 (2016) 101071–101078.
[79] Y. Nishiyama, Y. Nakagawa, N. Mizuno, High turnover numbers for the catalytic selective epoxidation of alkenes with 1 atm of molecular oxygen, Angew. Chem. Int. Ed. 40 (2001) 3639–3641.
[80] S.S. Mahajan, M.M. Sharma, T. Sridhar, Uncatalyzed oxidation of cyclooctene, Ind. Eng. Chem. Res. 44 (2005) 1390–1395.
[81] G. Grigoropoulou, J.H. Clark, J.A. Elings, Recent developments on the epoxidation of alkenes using hydrogen peroxide as an oxidant, Green Chem. 5 (2003) 1–7.
[82] L.P. Qian, Z. Wang, E.V. Beletskiy, J.Y. Liu, H.J. dos Santos, T.H. Li, M.D. Rangel, M.C. Kung, H.H. Kung, Stable and solubilized active Au atom clusters for selective epoxidation of cis-cyclooctene with molecular oxygen, Nat. Commun. 8 (2017).
[83] U. Biermann, U. Bornscheuer, M.A.R. Meier, J.O. Metzger, H.J. Schäfer, Oils and fats as renewable raw materials in chemistry, Angew. Chem. Int. Ed. 50 (2011) 3854–3871.
[84] A. Campanella, E. Rustoy, A. Baldessari, M.A. Baltanás, Lubricants from chemically modified vegetable oils, Bioresour. Technol. 101 (2010) 245–254.
[85] D.Y. Ok, N. Jiang, E.A. Prasetyanto, H. Jin, S.E. Park, Epoxidation of cyclic-olefins over carbon template mesoporous TS-1, Microporous Mesoporous Mater. 141 (2011) 2–7.
[86] M.M. Heravi, T.B. Lashaki, N. Poorahmad, Applications of Sharpless asymmetric epoxidation in total synthesis, Tetrahedron: Asymmetry 26 (2015) 405–495.

Supporting Information for

Multilamellar and Pillared Titanium Silicalite-1 with Long-Range Order of Zeolite Nanosheet Layers: Synthesis and Catalysis

Wei Wu[†], Dat T. Tran[‡], Xianyuan Wu[ǀ], Su Cheun Oh[†], Manyun Wang[§], Huiyong Chen[§], Laleh Emdadi[‡], Junyan Zhang[†], Emily Schulman[†], and Dongxia Liu[†*]

[†]Department of Chemical and Biomolecular Engineering, University of Maryland, College Park, MD, 20742, USA

[‡]U. S. Army Research Laboratory, RDRL-SED-E, 2800 Powder Mill Road, Adelphi, MD, 20783, USA

[ǀ]Institute of Industrial Catalysis, Zhejiang University of Technology, Hangzhou, China

[§]School of Chemical Engineering, Northwest University, Xi'an, Shaanxi, 710069, China

*Corresponding author:
Prof. Dongxia Liu
Email: liud@umd.edu
Phone: (+1) 301-405-3522
Fax: (+1) 301-405-0523

S1. Synthesis of TS-1 zeolites

1.1 Compositions for synthesis of M-TS-1 zeolites

Table S1. Compositions for synthesis of M-TS-1 zeolites using the general recipe of $100SiO_2/xC_6DN/yC_{22\text{-}6\text{-}6}/zTiO_2/6000H_2O/30BuOH$/m days.

Zeolite	**Composition in molar ratios**						
	SiO_2	**C_6DN (x)**	**$C_{22\text{-}6\text{-}6}$ (y)**	**TiO_2 (z)**	**H_2O**	**BuOH**	**Time (*m* days)**
M-TS-1 (0-7-1-10)	100	0	7	1	6000	30	10
M-TS-1 (30-7-1-10)	100	30	7	1	6000	30	10
M-TS-1 (60-7-1-10)	100	60	7	1	6000	30	10
M-TS-1 (120-7-1-10)	100	120	7	1	6000	30	10
M-TS-1 (60-7-2-10)	100	60	7	2	6000	30	10
M-TS-1 (60-7-3-10)	100	60	7	3	6000	30	10
M-TS-1 (60-7-4-10)	100	60	7	4	6000	30	10
M-TS-1 (60-1-1-10)	100	60	1	1	6000	30	10
M-TS-1 (60-4-1-10)	100	60	4	1	6000	30	10
M-TS-1 (60-9-1-10)	100	60	9	1	6000	30	10
M-TS-1 (60-7-1-2)	100	60	7	1	6000	30	2
M-TS-1 (60-7-1-5)	100	60	7	1	6000	30	5
M-TS-1 (60-7-1-7)	100	60	7	1	6000	30	7

1.2 Synthesis of conventional TS-1 (C-TS-1) zeolite

The C-TS-1 sample was prepared following the recipe reported by Zhang, H. *et al* [1]. In the synthesis, 10.00 g TEOS was added into a TPAOH aqueous solution that was prepared by mixing 3.59 g 40wt% TPAOH with 10.54 g DI water. After 50 min stirring, 0.16 g TBOT in 0.74g isopropanol solution was added into above mixture dropwise under stirring. The mixture was heated to 353 K under stirring to remove isopropanol. The molar composition of the zeolite precursor was $100SiO_2/15TPAOH/1TiO_2/1500H_2O$. Finally, the obtained zeolite synthesis gel was transferred into a Teflon-lined autoclave and placed in a convective oven at 443 K for 3 days under static condition. After crystallization, the zeolite sample was centrifuged, washed with DI water, and dried at 343 K overnight. The as-synthesized C-TS-1 sample was calcined using the same procedure as described for P-TS-1 zeolite.

S2. Textural properties of C-TS-1, M-TS-1 and P-TS-1 zeolite samples

Table S2. Textural properties of TS-1 zeolite samples determined from N_2 adsorption-desorption isotherms.

Zeolite	V_{micro}[a] (cm^3g^{-1})	S_{micro}[a] (m^2g^{-1})	S_{BET}[b] (m^2g^{-1})	S_{ext}[c] (m^2g^{-1})	V_t[d] (cm^3g^{-1})	V_{meso}[e] (cm^3g^{-1})	Si/Ti ratio[f]
M-TS-1 (0-7-1-10)	0	0	118	118	0.283	0.283	56
M-TS-1 (30-7-1-10)	0.031	51	242	190	0.427	0.396	81
M-TS-1 (60-7-1-10)	0.113	263	466	203	0.452	0.339	101
M-TS-1 (120-7-1-10)	0.117	270	514	244	0.788	0.671	104
M-TS-1 (60-7-2-10)	0.108	258	432	174	0.362	0.254	52
M-TS-1 (60-7-3-10)	0.106	247	416	170	0.354	0.248	40
M-TS-1 (60-7-4-10)	0.082	186	357	171	0.336	0.254	26
M-TS-1 (60-1-1-10)	0	0	106	106	0.198	0.198	125
M-TS-1 (60-4-1-10)	0.103	248	399	151	0.312	0.209	110
M-TS-1 (60-9-1-10)	0.105	256	410	153	0.308	0.203	111
M-TS-1 (60-7-1-2)	0	0	559	559	1.365	1.365	111
M-TS-1 (60-7-1-5)	0.106	244	498	254	0.435	0.329	107
M-TS-1 (60-7-1-7)	0.111	249	474	225	0.417	0.306	107
C-TS-1	0.159	391	464	73	0.236	0.077	108
P-TS-1	0.118	120	595	475	0.521	0.403	147

[a] *Determined from t-plot method;* [b] *Determined from Brunauer, Emmett, and Teller (BET) method;* [c] *Calculated by* $S_{ext} = S_{BET} - S_{micro}$; [d] *Calculated by* N_2 *adsorption at* $P/P_0 = 0.95$; [e] *Determined from* $V_{meso} = V_t - V_{micro}$; [f] *Determined by ICP-OES analysis.*

S3. M-TS-1 zeolites synthesized at different conditions

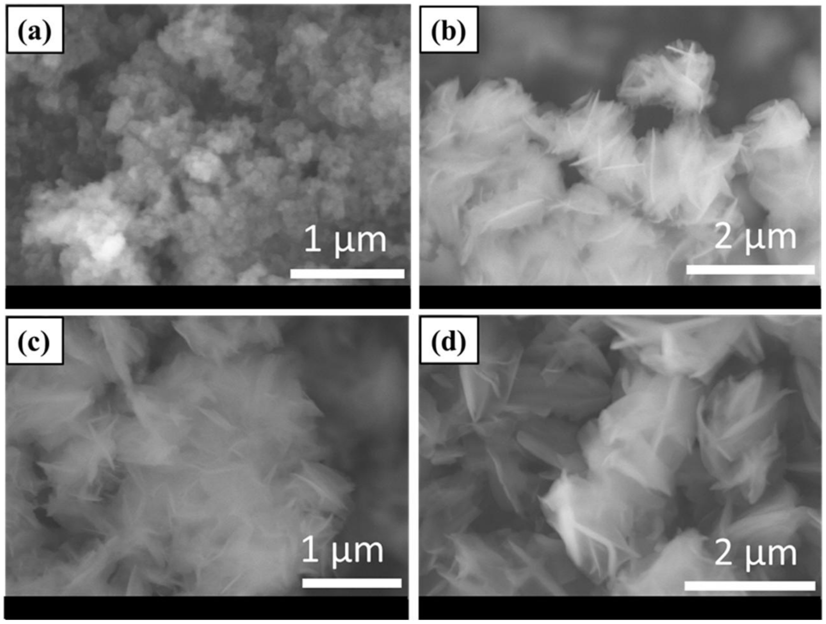

Figure S1. SEM images of (a) M-TS-1(60-1-1-10), (b) M-TS-1(60-4-1-10) and (d) M-TS-1(60-9-1-10), respectively, synthesized by using different $C_{22-6-6}Br_2$ concentrations. The SEM image of (c) M-TS-1(60-7-1-10) is represented here for comparison purpose.

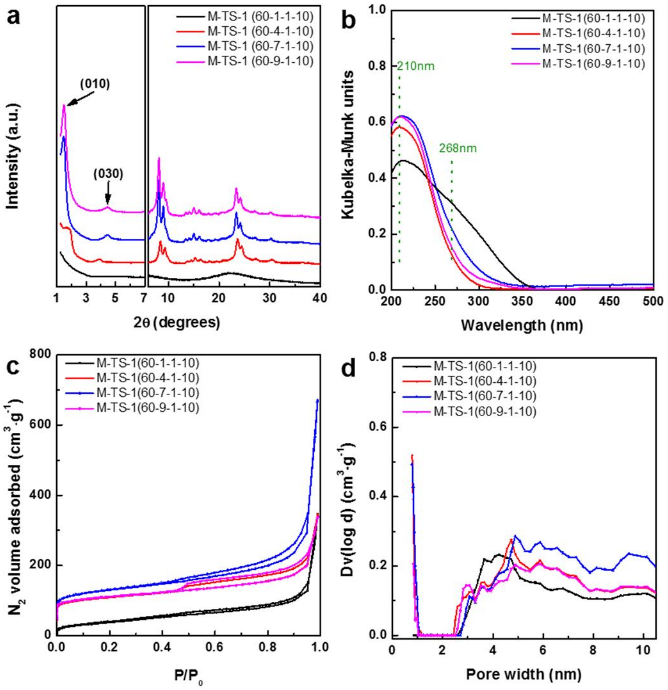

Figure S2. (a) Low- and high-angle XRD patterns, (b) DR UV-Vis spectra, (c) N_2 isotherms and (d) NLDFT pore size distributions of M-TS-1 sample synthesized by using different $C_{22-6-6}Br_2$ concentrations. The characterization data M-TS-1(60-7-1-10) is represented in each plot for comparison purpose.

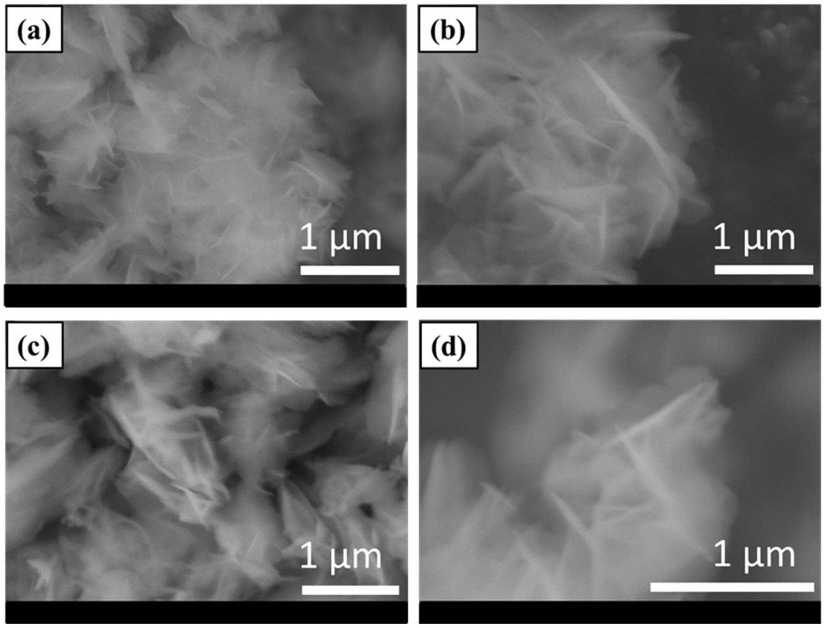

Figure S3. SEM images of (b) M-TS-1(60-7-2-10), (c) M-TS-1(60-7-3-10) and (d) M-TS-1(60-7-4-10), respectively, synthesized by using different TBOT concentrations. The SEM image of (a) M-TS-1(60-7-1-10) is represented here for comparison purpose.

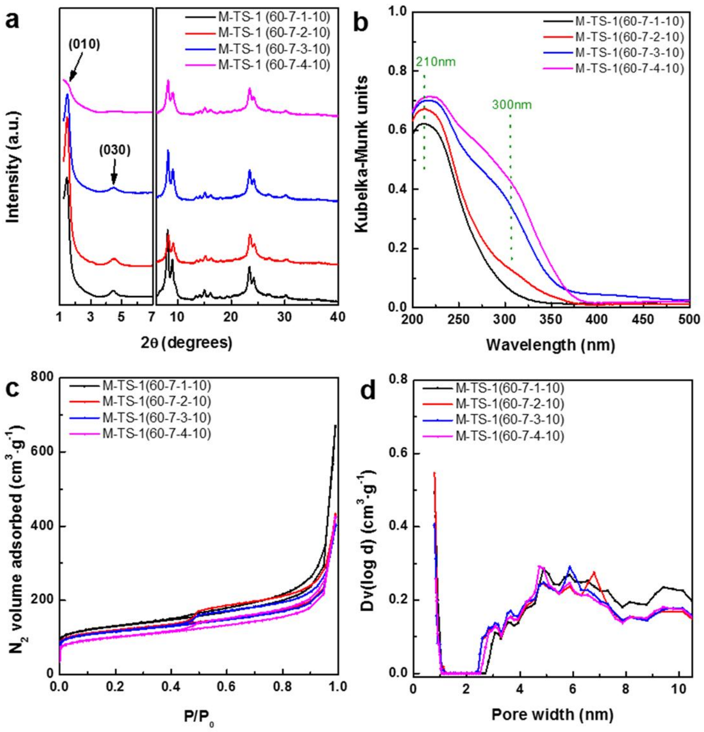

Figure S4. (a) Low- and high-angle XRD patterns, (b) DR UV-Vis spectra, (c) N_2 isotherms and (d) NLDFT pore size distributions of M-TS-1 samples prepared from the synthetic gel containing different TBOT concentrations. The characterization data M-TS-1(60-7-1-10) is represented in each plot for comparison purpose.

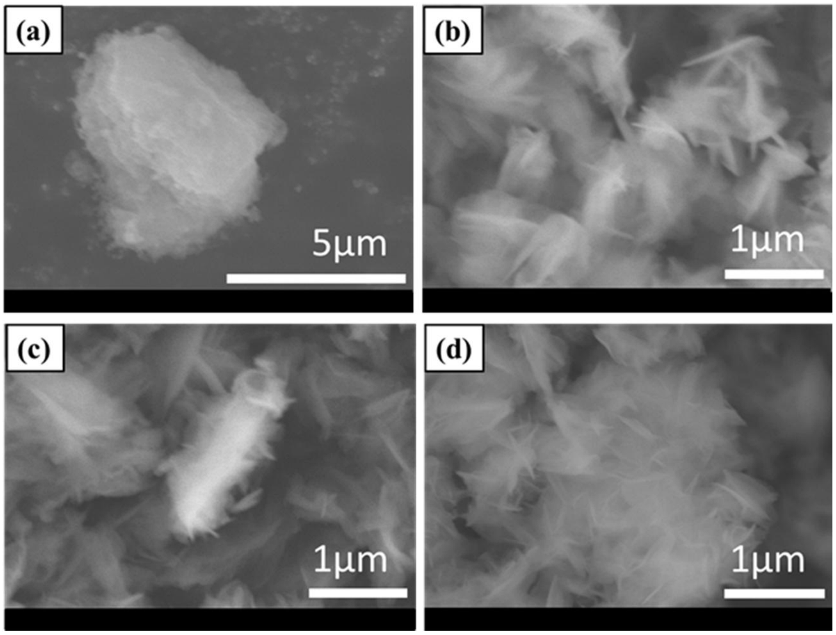

Figure S5. SEM images of (a) M-TS-1(60-7-1-2), (b) M-TS-1(60-7-1-5) and (c) M-TS-1(60-7-1-7), respectively, synthesized at different hydrothermal growth time. The SEM image of (d) M-TS-1(60-7-1-10) is represented here for comparison purpose.

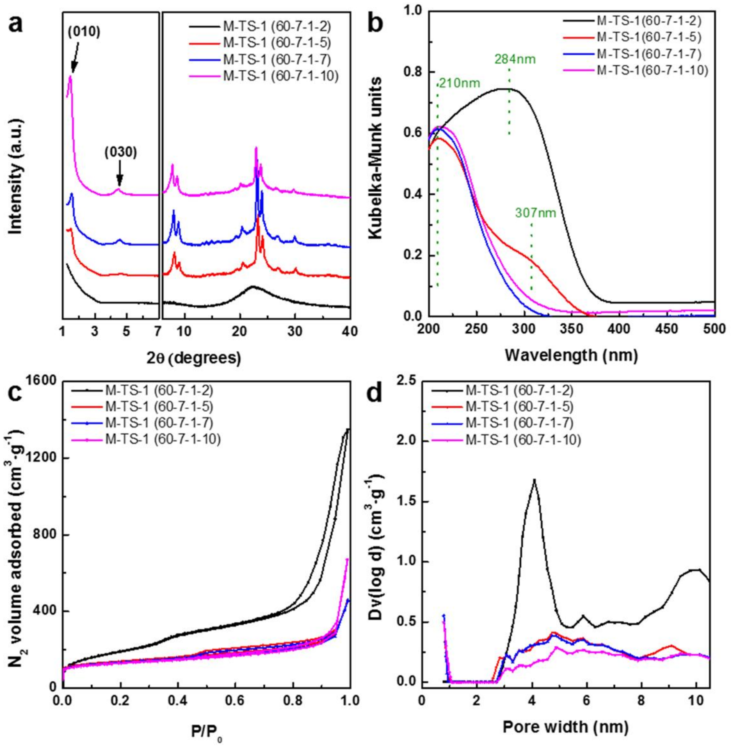

Figure S6. (a) Low- and high-angle XRD patterns, (b) DR UV-Vis spectra, (c) N_2 isotherms and (d) NLDFT pore size distributions of M-TS-1 samples synthesized at different hydrothermal growth time. The characterization data M-TS-1(60-7-1-10) is represented in each plot for comparison purpose.

S4. TEM images of M-TS-1(60-7-1-10) and P-TS-1 zeolites

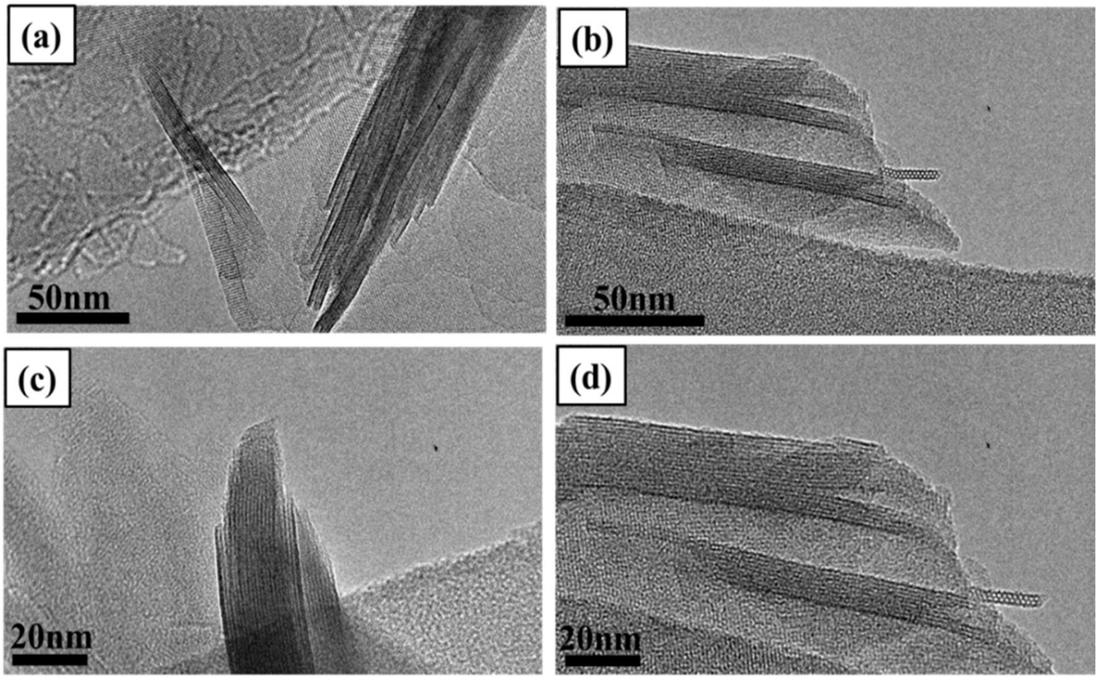

Figure S7. TEM images of M-TS-1 (60-7-1-10) zeolite.

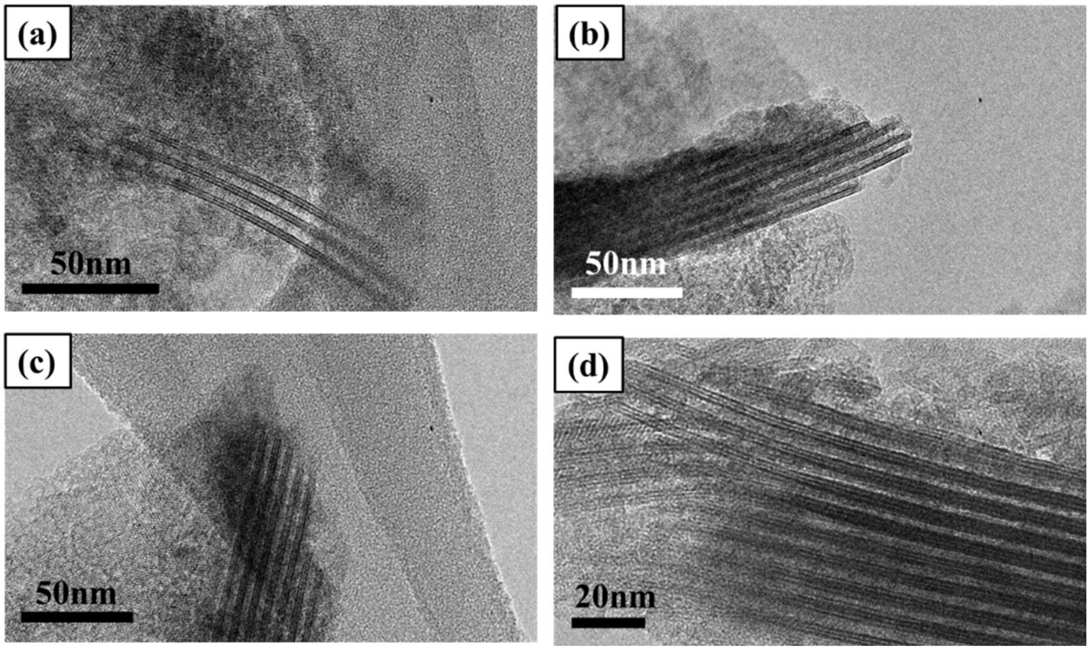

Figure S8. TEM images of P-TS-1 zeolite.

S5. Catalysis test results

(1) Representative GC micrographs in product analysis

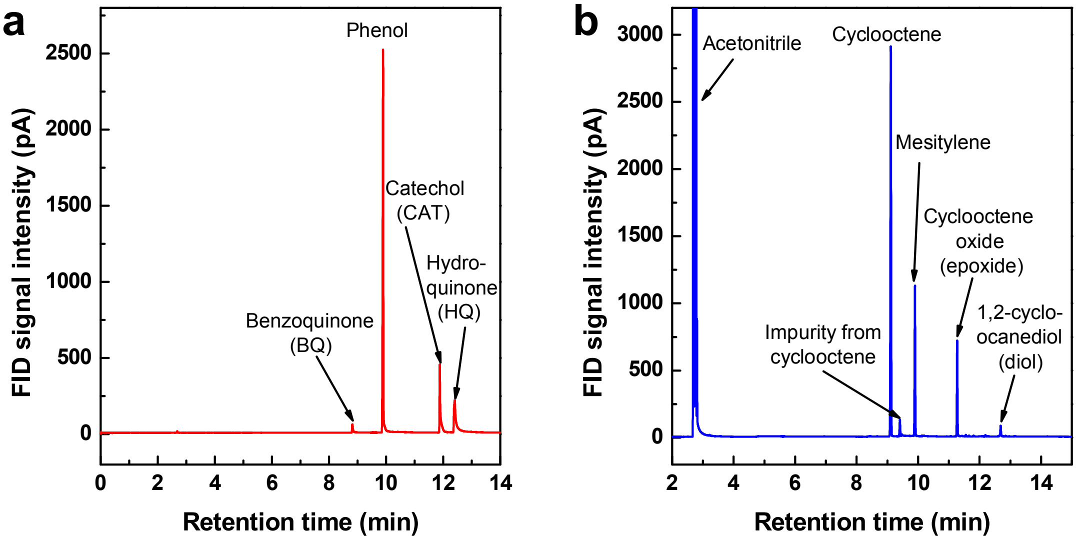

Figure S9. GC chromatograms for (a) phenol hydroxylation and (b) cyclooctene epoxidation.

(2) Performance of C-TS-1 in phenol hydroxylation and cyclooctene epoxidation

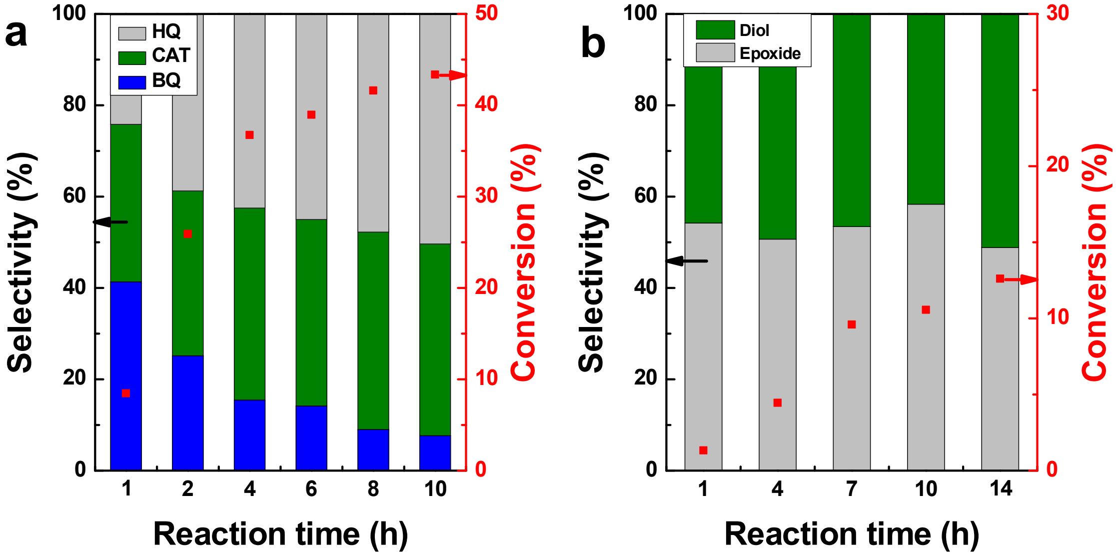

Figure S10. (a) Phenol conversion and product selectivity over C-TS-1 catalyst as a function of reaction time. (b) Cyclooctene conversion and product selectivity over C-TS-1 catalyst as a function of reaction time.

(3) Catalytic performance of C-TS-1, M-TS-1 and P-TS-1 with different Si/Ti ratio in phenol hydroxylation reaction

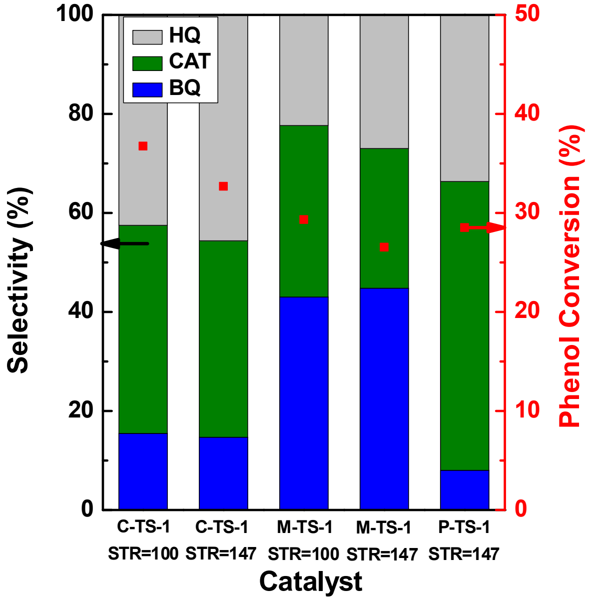

Figure S11. Phenol conversion and product selectivity over C-TS-1, M-TS-1 and P-TS-1 with Si/Ti ratio (STR) of 147. The reaction data obtained from C-TS-1 and M-TS-1 with STR of 100 are represented here for comparison purpose. (Reaction condition: 353 K, 50 mg catalyst, 500 mg phenol, 600 mg H_2O_2, 10 mL DI water, 4 h reaction time)

Reference

[1] H. Zhang, Y. Liu, Z. Jiao, M. He, P. Wu, Hydrothermal Synthesis of Titanium Silicalite-1 Structurally Directed by Hexamethyleneimine, Ind. Eng. Chem. Res., 48 (2009) 4334-4339.